Defect Chemistry of Oxide Nanomaterials with High Surface Area: Ordered Mesoporous Thin Films of the Oxygen Storage Catalyst CeO_2-ZrO_2

Pascal Hartmann,[†] Torsten Brezesinski,[†,§] Joachim Sann,[†] Andriy Lotnyk,[‡,⊥] Jens-Peter Eufinger,[†] Lorenz Kienle,[‡] and Jürgen Janek[†,*]

[†]Physikalisch-Chemisches Institut, Justus-Liebig-Universität, Heinrich-Buff-Ring 58, 35392 Giessen, Germany and [‡]Technische Fakultät, Christian-Albrechts-Universität zu Kiel, Kaiserstrasse 2, 24143 Kiel, Germany. [§]Present address: Institut für Nanotechnologie, Karlsruher Institut für Technologie, Hermann-von-Helmholtz-Platz 1, 76344 Eggenstein-Leopoldshafen, Germany. [⊥]Present address: Leibniz-Institut für Oberflächenmodifizierung e.V. (IOM), Permoserstrasse 15, 04318 Leipzig, Germany.

ABSTRACT Herein we report the electrical transport properties of a series of ordered mesoporous ceria–zirconia ($Ce_xZr_{1-x}O_2$, referred to as mp-CZO) thin films with both a cubic structure of (17 ± 2) nm diameter pores and nanocrystalline walls. Samples over the whole range of composition, including bare CeO_2 and ZrO_2, were fabricated by templating strategies using the large diblock copolymer KLE as the structure-directing agent. Both the nanoscale structure and the chemical composition of the mesoporous materials were analyzed by a combination of scanning and transmission electron microscopy, grazing incidence small-angle X-ray scattering, X-ray photoelectron spectroscopy, and time-of-flight secondary ion mass spectrometry. The total conductivity as a function of the film composition, temperature, and oxygen partial pressure was measured using impedance spectroscopy. The mesoporous solid solutions of CeO_2-ZrO_2 prepared in this work showed a higher stability against thermal ripening than both binary oxides, making them ideal model systems to study both the charge transport properties and the oxygen storage at elevated temperatures. We find that the redox properties of nanocrystalline mp-CZO thin films differ significantly from those of bulk CZO materials reported in the literature and, therefore, propose a defect chemical model of surface regions.

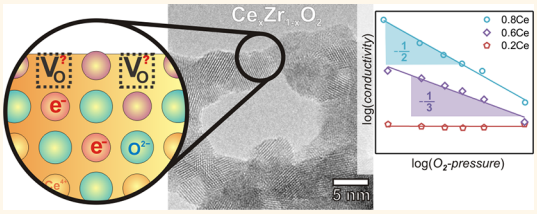

KEYWORDS: oxygen storage · heterogeneous catalysis · nanocrystalline solids · nanoionics · mesoporous · self-assembly · thin films

The term *defect chemistry* describes an established formal concept within solid state chemistry, which means the thermodynamic and kinetic control of point defect concentrations in crystalline functional materials. As the type and concentration of point defects are decisive for most physical properties of a crystalline material, defect chemistry forms today an important basis of materials science. Correspondingly, the typical strategy for designing functional ceramics is based on the choice of a suitable base compound and its tuning by compositional control and doping according to defect chemical concepts, if necessary.[1,2] The specific microstructure of polycrystalline materials, that is, the density and properties of grain boundaries and dislocations, adds further degrees of freedom to the design of such materials. Consequently, nanocrystalline ceramics with a maximum number of inner boundaries are being studied as their own class of interface-controlled materials, often exhibiting properties that differ significantly from those of microcrystalline samples.[3,4]

The concept of defect chemistry relies on the establishment of internal and external defect equilibria, such as by equilibrating a metal oxide like $CeO_{2-\delta}$ at elevated temperature in gas with a well-defined oxygen partial pressure. The oxygen deficiency δ, being a measure of the oxygen vacancy and electron concentration, is a function of the thermodynamic variables T and $p(O_2)$, and the defect-related properties can be

* Address correspondence to juergen.janek@phys.chemie.uni-giessen.de.

Received for review July 18, 2012 and accepted March 10, 2013.

Published online March 20, 2013
10.1021/nn400255w

© 2013 American Chemical Society

adjusted by reduction or oxidation in appropriate gas atmospheres.

From both fundamental and technological points of view, it is highly relevant to understand this redox behavior, in other terms, the point defect chemistry, of individual crystals as a function of their size, asking for the role of surfaces. Mesoporous materials, which are defined as solids with pore cavities ranging from 2 to 50 nm, can be prepared with a specific morphology and indeed are considered to hold great promise for numerous applications, such as energy conversion and storage, sensing, heterogeneous catalysis, photochromism, and so forth.[5−9] Ordered mesoporous materials can be seen best as a 3D network of short and interconnected crystalline "nanowires", typically showing a porosity of up to 70%. As is shown below, such materials enable access of the gas phase to each grain, thereby allowing direct and fast control of the physical properties by reaction with the gas phase. Considering the opportunities being offered by these materials,[10] it is surprising that up until now virtually no effort has been spent to systematically analyze their defect chemistry. One of the reasons for this might be the fact that the preparation of nanocrystalline thin film materials with a well-defined 3D pore structure still remains challenging. More critical is the fact that many mesoporous oxides are known to undergo significant restructuring during thermal annealing at elevated temperatures due to grain growth and sintering, and it may well be that the inherent thermodynamic instability of mesoporous networks does not allow the use of equilibrium concepts for the establishment of point defect equilibria. In order to explore the unique defect properties of mesoporous materials, first, one has to identify a suitable model system that can be synthesized with a well-defined mesostructure and further offers sufficient structural metastability at elevated temperatures. In addition, the bulk defect chemistry should already be well understood.

As demonstrated in this paper, solid solutions of the ternary system CeO_2-ZrO_2 perfectly fulfill these requirements. The binary compound ceria ($CeO_{2-\delta}$) is highly nonstoichiometric and is one of the most studied mixed-conducting oxides.[11,12] It has already been shown for dense nanocrystalline CeO_2 ceramics that the electrical conductivity is increased by orders of magnitude by decreasing the grain size to the nanoscale.[13] Detailed point defect models have been proposed to describe these "nanoionic" phenomena.[14−17] The binary compound zirconia (ZrO_2) in its monoclinic low-temperature phase is much less redox-active than CeO_2. Solid solutions with aliovalent oxides like Y_2O_3 or CaO crystallize in the cubic fluorite structure and are widely used as excellent oxygen ion conductors, for example, in solid oxide fuel cells (SOFC). As for CeO_2, the transport phenomena in nanocrystalline zirconia as well as along well-defined interfaces are extensively studied and transport models are being developed.[18,19]

From the 1990s on, ceria-based oxides found application as oxygen storage catalyst supports in automotive exhaust systems. During this period, the solid solution $Ce_xZr_{1-x}O_2$ was investigated in detail using diffraction and vibrational spectroscopic techniques, which ultimately led to a profound knowledge about the microstructural properties.[20] For oxygen storage applications, nanocrystalline $Ce_xZr_{1-x}O_2$ is of particular interest. In the past years, several studies on the phase formation and stability,[21] charge transport,[22] oxygen partial pressure sensing,[23] oxygen storage capability,[24,25] and environmental catalysis[26,27] have been published.

In the following, we introduce nanocrystalline mesoporous thin films of the solid solution CeO_2-ZrO_2 with a well-designed microstructure as model systems for the size-dependent study of defect chemical reactions. It is the major concern of this paper to prove that the solid solutions are, in contrast to the binary oxides, structurally and morphologically metastable at elevated temperatures which allows oxidation and reduction for the control of point defect concentrations and, thus, for the manipulation of electrical properties beyond the mere control of the mesoporous morphology.[28]

RESULTS AND DISCUSSION

First, we present a systematic study of both the mesoporous morphology and the nanocrystalline framework of solid solution thin films of $Ce_xZr_{1-x}O_2$ with six different compositions, namely, $x = 0$, 0.2, 0.4, 0.6, 0.8, and 1 (denoted as 0CZO, 2CZO, 4CZO, 6CZO, 8CZO, and 10CZO, respectively). All materials were characterized by various state-of-the-art techniques, including EDS, XPS, ToF-SIMS, HRSEM, STEM, XRD, and GISAXS. We show that the mesoporous oxide films are thermally highly stable and keep their morphology and crystalline structure up to temperatures as high as 600 °C for several hours. This allowed studying the influence of the thermodynamic variables temperature and oxygen partial pressure on the charge transport properties without disturbance by Ostwald ripening or structure collapse. We found that the redox properties of mp-CZO are quite different from the known properties of micro- or single-crystalline CZO and propose a simple point defect model for the interpretation of the results. To the best of our knowledge, no comparable approach has been reported so far.

Nano- and Microstructure. Figure 1 shows typical electron microscopy images of mp-CZO thin films after removal of the diblock copolymer and crystallization of the initially amorphous wall structure at 600 °C. The high-magnification top view SEM image in panel A reveals an ordered network of open pores (17 ± 2) nm in diameter at the solid−air interface. The in-plane pore-to-pore distance is estimated to (25 ± 2) nm, which

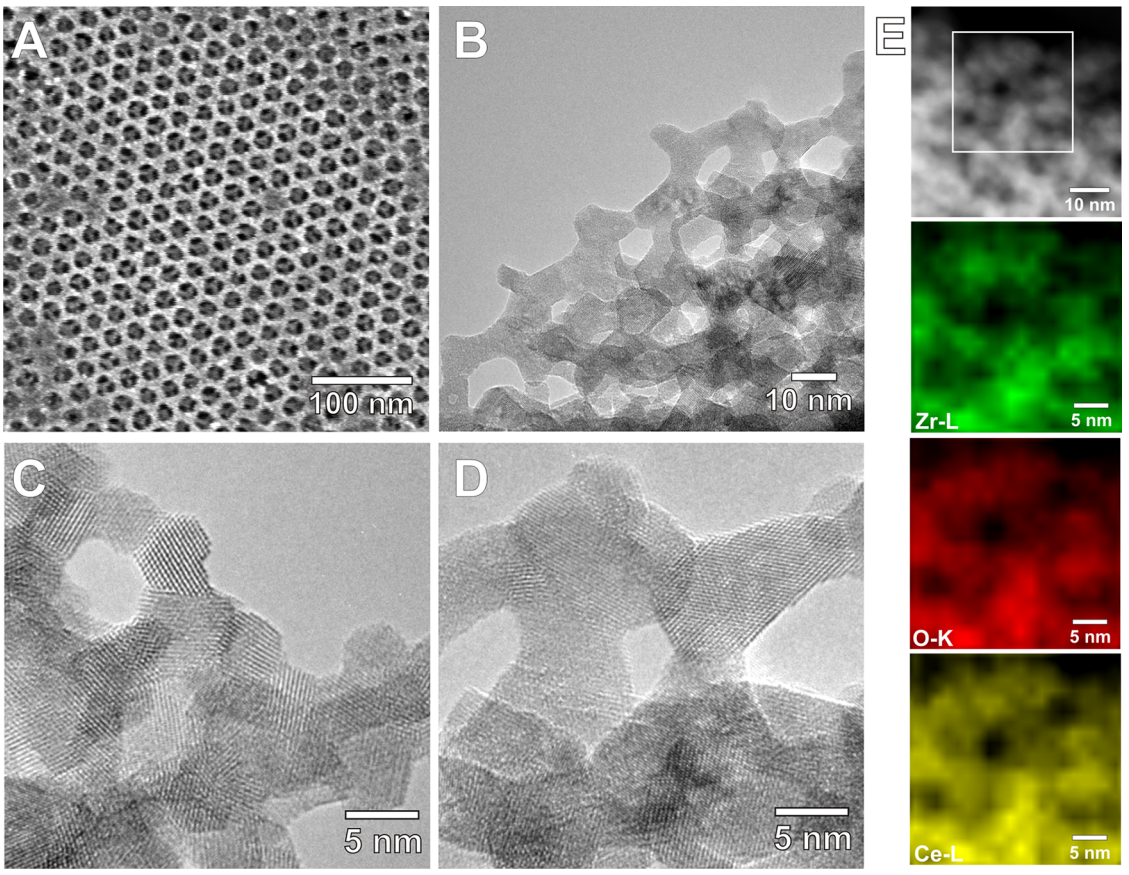

Figure 1. SEM (A) and TEM (B) images showing the cubic pore structure of mp-CZO thin films heated at 600 °C in air. HRTEM images of 8CZO (C) and 2CZO (D) confirming the nanocrystalline nature of both solid solutions. (E) STEM-HAADF image of 8CZO with EDS elemental maps of O, Ce, and Zr of the region indicated by the square.

leads to wall thicknesses of (4−12) nm. Overall, we find that samples with high cerium content tend to have thinner walls, while samples with a low content exhibit thicker walls. The thickness of the films was determined by cross-sectional SEM (not shown) to be (110−140) nm.

In addition to SEM, both high-resolution TEM (HRTEM) and scanning TEM (STEM) images were collected for all materials prepared in this work. These data are generally consistent with the SEM observations and provide further insight into the microstructure, including crystallite size and shape. Panels B−D of Figure 1 show representative TEM images at different magnifications (see also HRTEM images in Figure S1 and STEM images in Figures S2−S5 in Supporting Information). HRTEM studies indicate that the inorganic walls of samples 4CZO−10CZO consist of crystallites with almost spherical shape. For 10CZO, crystalline domain sizes of (5−8) nm are observed. By contrast, the 8CZO, 6CZO, and 4CZO solid solutions reveal crystallites averaging (3−6) nm in diameter. For materials with a low cerium content (here 2CZO and 0CZO), we find more elongated crystallites with a bar-type shape. These samples also showed significantly larger domains ranging from (5−8) nm and (9−17) nm for the short side and (8−15) nm and (20−30) nm for the long side, respectively. Overall, HRTEM confirms that the mesoporous framework of the different samples consists of highly crystalline nanodomains after thermal annealing at 600 °C (500 °C for 0CZO); no amorphous regions were observed. In addition, STEM and EDS mapping data establish the homogeneous distribution of Ce, Zr, and O throughout the bulk of the films. This means that the formation of either Ce-rich or Zr-rich domains due to phase separation at the nanoscale or fluctuation in composition can be ruled out (see Figure 1E). We note that Mamontov *et al.* report nanoscale concentration heterogeneities in nanocrystals of $Ce_{0.5}Zr_{0.5}O_2$, which may originate from treatments at higher temperatures up to 800 °C.[29]

Apart from electron microscopy, we also used grazing incidence small-angle X-ray scattering (GISAXS) to probe the pore structure of the polymer-templated $Ce_xZr_{1-x}O_2$ thin films. Figure 2 shows typical *ex situ* GISAXS patterns at an angle of incidence $\beta = 0.2°$ for materials with both fully amorphous and highly crystalline walls. From the data obtained after thermal annealing at 300 °C, it is apparent that both the solid solutions and the bare CeO_2 produce patterns with distinct maxima. These scattering maxima can be indexed to distorted face-centered cubic (fcc) pore structures with (111) orientation relative to the plane of the substrate.

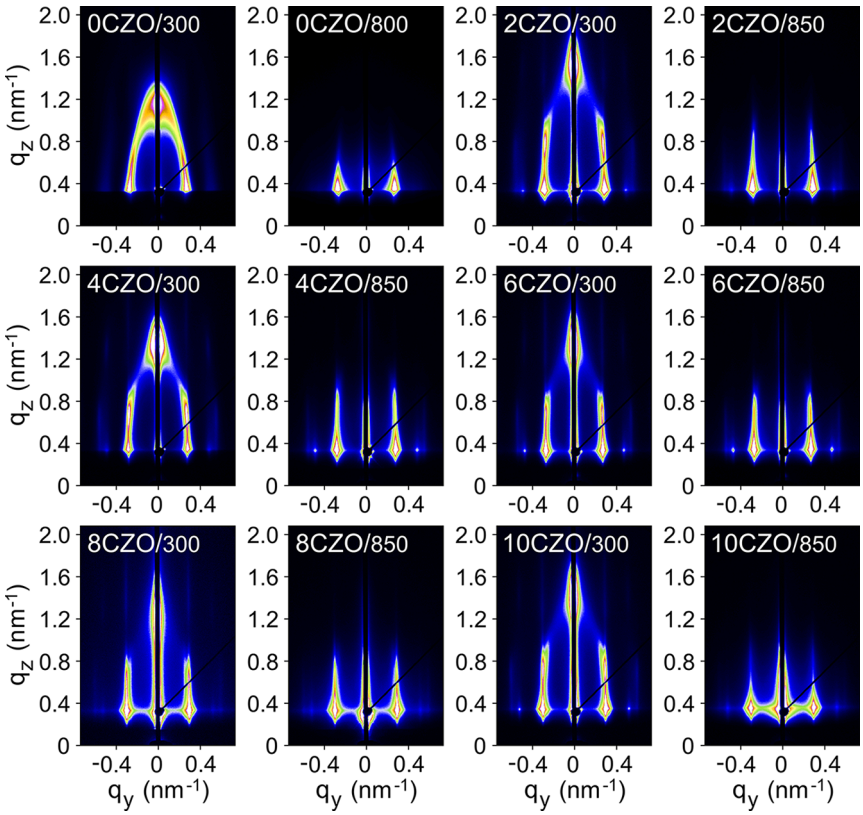

Figure 2. Synchrotron-based GISAXS at an angle of incidence β = 0.2° on polymer-templated $Ce_xZr_{1-x}O_2$ thin films. The acronyms on the top left corner of each panel represent the chemical composition and the corresponding annealing temperature (here 300 °C for 12 h and 800 and 850 °C for 1 min). It should be noted that 0CZO was only heated at 800 °C because higher annealing temperatures led to the complete loss of in- and off-plane scattering.

We note that this kind of pore structure is quite often found for KLE-templated oxide thin films and is further consistent with the hexagonal symmetry of the top surface (see Figure 1A).[30,31] In contrast, the GISAXS pattern for ZrO_2 only shows diffuse maxima, which do not allow for a differentiation between the possible cubic crystal structures. The finding that ZrO_2 thin films exhibit both a lower degree of periodicity and a lower preferred orientation is likely a direct result of the different hydrolysis and condensation rates of the molecular zirconium and cerium species. The elliptical shape of the GISAXS patterns further indicates a large unidirectional lattice contraction. On the basis of the relative position of the (111) scattering maxima, a decrease in film volume of more than 70% is determined for samples heated at 300 °C. At first glance, such contraction in the off-plane direction (*z*-direction) seems rather large but is not surprising in view of the sol–gel processing. Higher annealing temperatures only lead to a minor further contraction presumably because the chloride salt precursors employed in this work are fully decomposed by 300 °C.

From the GISAXS patterns in Figure 2, it can also be observed that annealing temperatures of 800 °C and 850 °C lead to the loss of off-plane scattering. This loss is due both to the morphological anisotropy of the thin films with significantly fewer repeat units normal to the plane of the substrate and to the crystallization process itself. The latter may slightly disrupt the nanoscale structure. However, the results with GISAXS establish that the distorted networks of pores are retained when the crystalline phase is achieved. In addition, it is evident that 4CZO, 6CZO, and 8CZO exhibit the highest thermal stability of all samples studied here because even the off-specular scattering maxima are retained to a certain extent after 850 °C. We note that these mesoporous materials can withstand annealing temperatures as high as 950 °C for a short time (see Figure S6 in Supporting Information). Lastly, we want to emphasize that the solid solutions can be heated at both 550 °C and 650 °C for several hours without severely disrupting the nanoscale structure due to grain growth, sintering, and so forth (see Figure S7 in Supporting Information). This result underlines the exceptional thermal stability of the mp-CZO thin films.

In the following, we specifically focus on samples that were heated at 600 °C for 1 h (500 °C for 0CZO). Part of the reason for this is the apparent high crystallinity and the fact that the nanoscale structure is still well-defined.

Figure 3A shows wide-angle X-ray diffraction (WAXD) patterns for all mp-CZO thin films. The diffractogram at the bottom is from the bare Si(100) substrate. It should be noted that the strong peak at

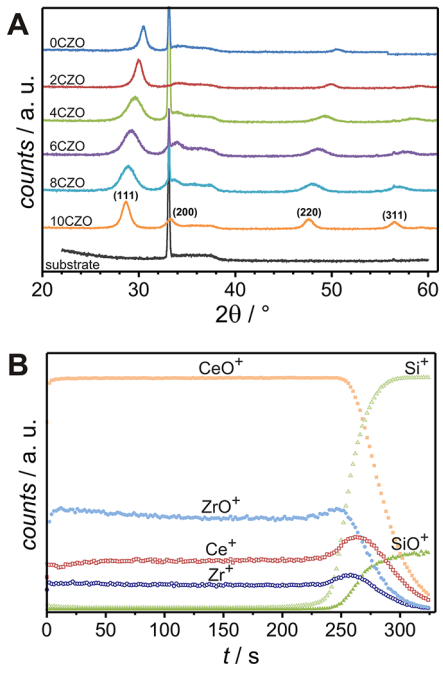

Figure 3. WAXD patterns (A) of mp-CZO thin films after thermal annealing at 600 °C for 1 h. ToF-SIMS depth profiles (B) of a 140 nm thick mp-CZO thin film on a Si(100) substrate.

$2\theta \approx 33.1°$ is also found in the WAXD patterns of the different CZO materials. Apart from substrate signals, all patterns show four distinct reflections. For CeO_2 (10CZO), both peak positions and relative intensities are in agreement with the JCPDS (Joint Committee on Powder Diffraction Standards) reference data for CeO_2 with CaF_2 structure (no. 34-0394). The calculated lattice constant a is 5.39(1) Å, which is only approximately 0.4% smaller than that of bulk ceria. For ZrO_2 (0CZO), a clear assignment to a certain crystal phase is not possible on the basis of these data alone. The observed reflections may correspond either to the tetragonal phase or to the cubic phase. Significant amounts of monoclinic zirconia can be ruled out, however. JCPDS reference data for all three ZrO_2 phases are shown in Figure S8 (see Supporting Information). Solid solutions of CeO_2-ZrO_2 are known to exhibit a cubic cation sublattice, and the tetragonal symmetry originates from a displacement of anions in the oxygen sublattice.[32] Lamas *et al.* probed nanocrystalline $Ce_xZr_{1-x}O_2$ materials by synchrotron-based X-ray diffraction to detect the weak scattering of the displaced oxygen anions. They explained the appearance of the (112) reflection in 1.5CZO−7CZO with the tetragonal crystal symmetry. In contrast, for 8CZO and 10CZO, they found cubic symmetry.[21] For the solid solutions, we find that the peak positions shift toward lower 2θ values with increasing cerium content. As the ionic radius of Ce^{4+} (97 pm) is approximately 20% larger than that of Zr^{4+} (84 pm), the lattice constant of CZO increases with increasing cerium content, which ultimately leads to the peak shift observed in the WAXD patterns.[33]

Moreover, the full width at half-maximum (fwhm) intensity seems to be a function of composition; the greatest widths are observed for 4CZO, 6CZO, and 8CZO. This indicates that in solid solutions smaller crystallites are formed under otherwise identical conditions. A rough estimate can be obtained from Scherrer analysis which relates the fwhm intensity of peaks to the physical dimension of the scattering domains.[34] Such analysis provides domain sizes of approximately 8 nm for 10CZO, (4−5) nm for 8CZO, 6CZO, and 4CZO, (8−9) nm for 2CZO, and (9−12) nm for 0CZO. For mp-CZO thin films with high cerium content, these values are consistent with those determined by HRTEM imaging. By contrast, for both 2CZO and 0CZO, there is a certain discrepancy likely due to the different shape of the crystallites (spherical for 4CZO−10CZO and elongated for 2CZO and 0CZO). Apart from the smaller size of the crystallites, the solid solutions showed a significantly higher thermal stability than both bare CeO_2 and ZrO_2. This result is not surprising, however, because it is known that diffusion of cations in CeO_2-ZrO_2 materials is strongly suppressed due to the large difference in cation radii. For example, Pijolat *et al.* showed that the addition of only 3 atom % of Zr^{4+} to CeO_2 leads to a reduction in domain growth rate by a factor of approximately 10.[28] This makes the material a potential model system for defect chemistry studies in the oxygen sublattice, as such requires thermal treatment for equilibration over longer periods of time.

Chemical Composition and Bonding Configuration. The Ce/Zr molar ratios of the mp-CZO thin films were determined by energy-dispersive X-ray spectroscopy (EDS). Typical EDS spectra for 4CZO and 6CZO are shown in Figure S9 (see Supporting Information). Apart from cerium, zirconium, and oxygen, only silicon and carbon, with the latter in very small amounts, were detected. The comparatively strong silicon signal results from the underlying Si(100) substrate. The deviation between the measured Ce/Zr ratios and those predicted from the synthesis recipes range from 0% to 10%, depending on the material composition. For 2CZO and 6CZO, EDS spectra were also taken from different film positions to examine the lateral homogeneity. These experiments confirm the in-plane homogeneity with deviations of only (0.5−5)%. Because most of the EDX signal results from the silicon substrate, these values are within the uncertainty of the method.

To obtain information about the film composition as a function of thickness, time-of-flight secondary ion mass spectrometry (ToF-SIMS) measurements were conducted on 140 nm thick mp-CZO samples (see Figure 3B). About 120 spectra were collected before reaching the Si(100) substrate, leading to a depth resolution of approximately 1 nm. From the ToF-SIMS data, it is evident that both the Si^+ and SiO^+ line intensities increase not before the CZO/substrate

interface is reached. This indicates that diffusion of silicon across the interior of the films at elevated temperatures can be largely ruled out. We also note that minor amounts of hydrocarbons can only be detected at the CZO/air interface, which implies that the KLE diblock copolymer is fully combusted after thermal annealing at 600 °C in air. Apart from the expected cations, we find trace amounts of Li^+, Na^+, and K^+. As opposed to cerium and zirconium, the ionization probability of these elements is large, and thus, comparatively strong secondary ion signals are found by default even though the samples contain only trace amounts. However, the concentration of alkaline earth cations, such as Ca^{2+} and Ba^{2+}, is negligible. Overall, the profiles collectively verify that the metal ions are homogeneously distributed throughout the bulk of the films and that no major impurities are present. Nevertheless, it should be noted that ToF-SIMS—despite a high spatial resolution—only provides a qualitative measure of the distribution of elements.

From both EDS and ToF-SIMS analyses, we obtained information about the local composition of the different samples. However, the chemical environment of the elements cannot be identified using these techniques. In particular, knowledge about the oxidation state of the cerium ions (usually 4+ or 3+ for partially reduced species) is very important to understand the materials properties. For this reason, we also conducted X-ray photoelectron spectroscopy (XPS) measurements on the various mp-CZO thin films. It should be noted that mesoporous materials, in general, represent a unique case for XPS because the pore wall thickness of (4−12) nm is pretty much on the same order of magnitude as the information depth of (2−10) nm. Therefore, we expect our data to be representative for the entire volume rather than just the surface, and since we know that the porous film is homogeneous throughout, the XPS analysis provides reliable information on the average composition of the entire film. The analysis of XPS data of ceria-based materials itself is challenging due to the complex Ce 3d spectra. Figure 4 shows typical Ce 3d spectra of samples with x = 0.2, 0.4, 0.6, 0.8, and 1.0. Because a detailed analysis needs powerful theory to account for both the hybridization and the partial occupancy of the Ce 4f orbitals, we used the generally accepted approach to fit the spectra with 10 lines in order to extract the Ce^{3+}/Ce^{4+} ratio and to see whether the composition has an effect on this ratio.[35,36] These 10 lines consist of five spin−orbit split pairs with a splitting of approximately 18.45 eV. During the fitting procedure, we coupled (i) the line positions (18.45 eV separation), (ii) the full widths at half-maximum (fwhm), and (iii) the area intensities (3:2) for each pair of lines. A linear background was subtracted from all spectra because this gave the best and most reliable fits to the data. The

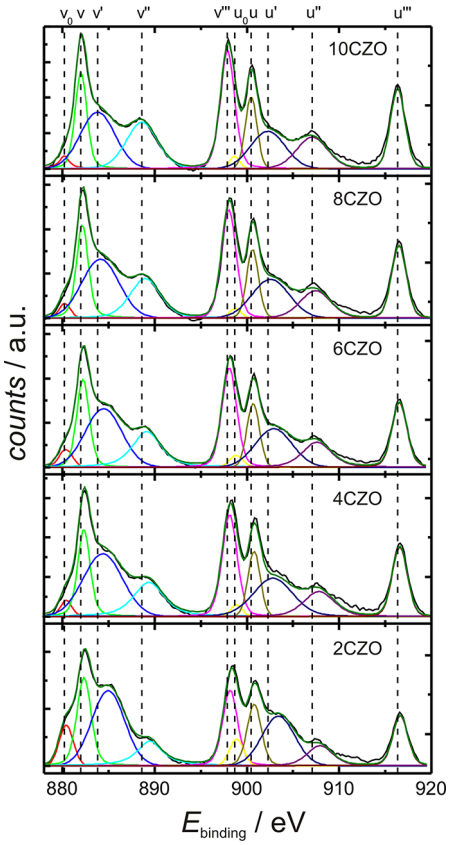

Figure 4. XPS detail spectra of the Ce 3d core level regions for all cerium-containing mp-CZO thin films. The experimental data are shown as black curves and fits to the data including sum of the peak fits as colored curves.

TABLE 1. Experimental Binding Energies and Full width at Half-Maximum (γ) of the Five Ce $3d_{5/2}$ Peaks

composition	v_0	γ	v	γ	v'	γ	v''	γ	v'''	γ
10CZO	880.20	1.26	882.01	1.50	883.81	4.43	888.62	3.99	897.89	1.86
8CZO	880.26	1.45	882.16	1.51	884.11	4.73	888.98	3.88	898.03	1.90
6CZO	880.36	1.73	882.23	1.61	884.46	4.67	889.14	3.69	898.09	1.90
4CZO	880.40	1.46	882.33	1.59	884.38	5.02	889.36	3.91	898.12	1.95
2CZO	880.39	1.75	882.32	1.81	884.91	4.30	889.49	3.22	898.18	1.94

$3d_{5/2}$ lines are denoted as v_0, v, v', v'', and v''', and the spin−orbit split $3d_{3/2}$ lines as u_0, u, u', u'', and u'''. The results for the $3d_{5/2}$ lines are given in Table 1; the $3d_{3/2}$ lines 18.45 eV higher in binding energies have the same fwhm.

From the area intensities of these peaks, the concentration of Ce^{3+} relative to the total Ce concentration is calculated using the following equation:

$$\frac{[Ce^{3+}]}{[Ce(total)]} = \frac{I(v_0) + I(v') + I(u_0) + I(u')}{I(total)}$$

The calculated fraction $[Ce^{3+}]/[Ce(total)]$ for bare CeO_2 (10CZO) is equal to 0.31, thereby indicating that the mesoporous material is already highly oxygen-deficient:[25] introducing this oxygen deficiency as nonstoichiometry δ, we can write CZO as $Ce_xZr_{1-x}O_{2-\delta}$ or

more precisely as $[(Ce^{3+})_{2\delta}(Ce^{4+})_{x-2\delta}Zr_{1-x}]O_{2-\delta}$. The nonstoichiometry δ and the fraction $[Ce^{3+}]/[Ce(total)]$ are both depicted in Figure 5. The calculation of δ is based on the assumption that the formation of two Ce^{3+} ions is compensated by the formation of one oxygen vacancy (*i.e.*, the release of one oxygen atom from the lattice; see description of the defect chemistry below).

We did not see changes in the spectra due to UHV or X-ray irradiation for exposure times shorter than 24 h, indicating that the material characterized under UHV does not differ significantly from the material characterized under ambient pressure. With increasing zirconium content, the fraction of Ce^{3+} increases at given $p(O_2)$. This observation clearly shows the preferred formation of oxygen vacancies in the vicinity of zirconium ions. However, the oxygen nonstoichiometry is the highest for pure ceria and the lowest for 2CZO. The oxygen deficiency takes values of almost 10% for films that were annealed in air under oxidizing conditions (600 °C). Such large oxygen deficiencies are only observed under highly reducing conditions for bulk materials,[37] and the unique redox properties of mp-CZO become plausible. The quantitative analysis of the O 1s peak with respect to the metal/O ratio is not possible, as the quantification is hampered by adsorbed C−O species. In addition, we observed that all lines shift to higher binding energies with increasing zirconium content; however, the v', v'', u', and u'' lines showed a larger shift of approximately 1 eV compared to approximately 0.25 eV for the other lines.

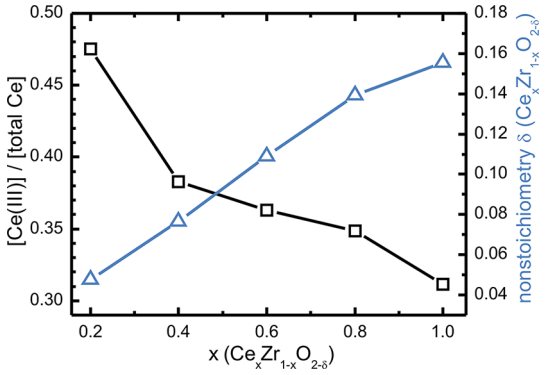

Figure 5. Plots showing the fraction of Ce^{3+} relative to the total Ce concentration (black squares) and the nonstoichiometry δ from XPS (blue triangles) as a function of film composition. It should be noted that the point connecting lines are not fits to the data.

Impedance Spectroscopy and Electrical Conductivity. As mentioned above, knowledge about the electrical conductivity of $Ce_xZr_{1-x}O_2$ materials is important for many applications, including sensors and fuel cell cathodes. More importantly, it is also a direct measure of the redox state since the number of electronic and ionic charge carriers depends sensibly on the oxygen deficiency. This might be of direct use for application, as recently the wireless measurement of the electrical conductivity of CZO catalysts has been tested for the monitoring of the catalyst oxidation state.[38] Thus, we examined the conductivity of the different mp-CZO thin films as a function of the film composition, temperature, and oxygen partial pressure. The in-plane film resistance (*i.e.*, parallel to the plane of the substrate) was measured using two-probe impedance spectroscopy. Figure 6 shows Nyquist plots (imaginary part *vs*

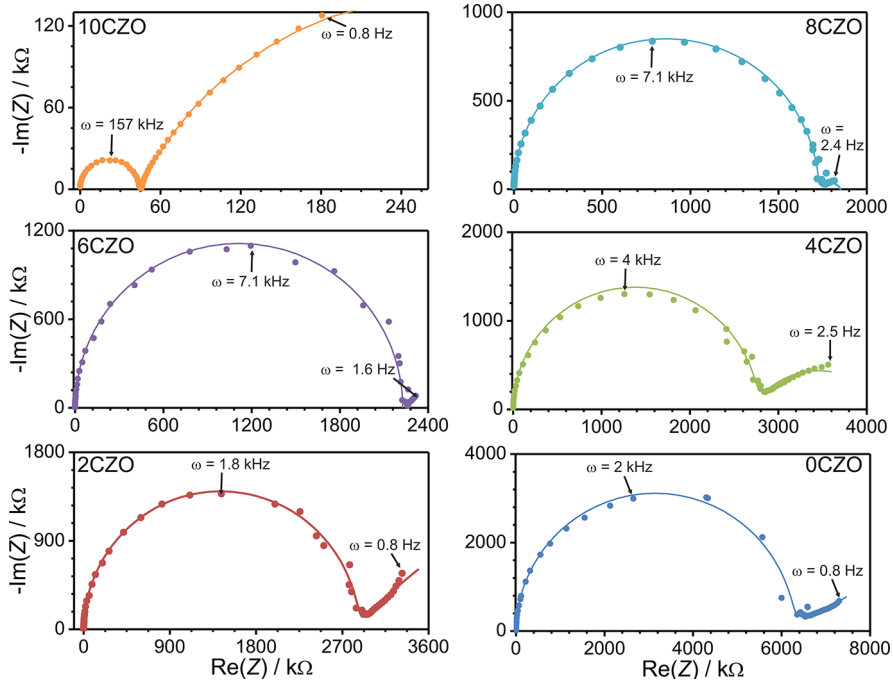

Figure 6. Nyquist representations of impedance data measured at 450 °C in air. Lines represent simulated impedance spectra using parallel *RC* circuits.

real part of impedance) for all samples measured at 450 °C in air. From these data, it can be clearly seen that the mesoporous materials show an almost ideal semicircle at high frequencies (1 kHz < ω < 1 MHz), which can be described by an equivalent circuit of an ohmic resistance in parallel to a capacitance (parallel *RC* circuit). The ohmic resistance depends on the sample composition and is equal to the diameter of the semicircle. The smallest and largest resistances were found for bare CeO_2 and ZrO_2 with approximately 50 kΩ and 6200 kΩ, respectively. For the solid solutions, the values range from 1700 kΩ to 2900 kΩ. We note that the conductance of the quartz glass substrates used was also measured and found to be at least 2 orders of magnitude smaller than that of the mp-CZO thin films (for details see Figure S10B in Supporting Information). Figure S10A shows the absolute value of *Z* as a function of the excitation frequency *f* (Bode plot). Both the mp-CZO samples and the substrate show a linear increase of |*Z*| (slope ≈ −1) with similar values for decreasing frequencies from 10^6 Hz to approximately 10^4 Hz. This impedance behavior is characteristic of an ideal capacitance *C* described by a phase angle of −90°. The capacitance of the high-frequency semicircle was calculated to be approximately 10^{-10} F independent of the sample composition.

In the Nyquist representations (see Figure 6), the beginning of a second semicircle (parallel *RC* circuit) at high Re(*Z*) values, equivalent to low frequencies, can be observed. For all materials, the capacitance was determined to be approximately 10^{-6} F; a nonideal capacitance simulated by a constant phase element (CPE) was used to fit the data. However, the resistance varied significantly among the different samples. In the Bode plots in Figure S10A, the beginning of the second *RC* circuit is indicated by a rise of |*Z*| at low frequencies. Because of the logarithmic scaling of |*Z*|, this rise can only be seen clearly if there is a significant relative change in |*Z*|, as for CeO_2.

The lowest capacitances in ceramic systems are typically observed for the grain interior or the geometric capacitance of the sample investigated.[39] In a typical thin film cell arrangement (similar to that used in this work), this capacitance is very small compared to the capacitance of the substrate and sample holder in parallel (see Figure S10A). Because the measured high-frequency capacitance of the bare glass substrate is similar to that of the thin film materials, the capacitive behavior is most likely determined by both the substrate and the sample holder.[40]

The highest capacitances are typically observed at electrolyte−electrode interfaces or solid−solid heterojunctions, and therefore, we attribute the low-frequency *RC* circuit to the impedance response of the Pt electrode/CZO interface.[39] The capacitance is related to the double layer of electrical charges at this interface, while the resistance is related to the transfer of electrical charges through this interface. It should be noted that the interdigitated microelectrodes on top of the mp-CZO thin films cannot be considered as an ideal cell arrangement (cube-like sample sandwiched between two plate electrodes). Tuller *et al.* studied patterned interdigitated Pt electrodes (similar to that used here) on fast oxygen ion conductor yttria-stabilized zirconia (YSZ) thin films.[41] They found an additional feature in the impedance spectra at low frequencies due to a so-called constriction resistance and proposed a more complex equivalent circuit to describe the electrode impedance data at low frequencies. However, we focus on the thin film resistance, that is, the high-frequency impedance behavior, which according to Tuller *et al.* shows an ideal behavior if the electrode distance is significantly larger than the film thickness (by a factor of 100). In the present work, an electrode distance of 20 μm is used and the film thickness is only approximately (100−140) nm. Consequently, we can rely on the conductivity data from the high-frequency resistance. Moreover, we note that an additional *RC* circuit for grain boundary transport is not observed.

We calculated the conductivity of the mp-CZO thin films using the resistance *R* of the high-frequency *RC* semicircle and the film geometry while neglecting the nanoscale porosity. One should keep in mind that considering the sample as a dense ceramic thin film always leads to an underestimation of the conductivity values of the solid phase. The conductivity given here is the mean value for the solid phase and pore network. Figure 7A shows the conductivity values as a function of film composition for three different temperatures,

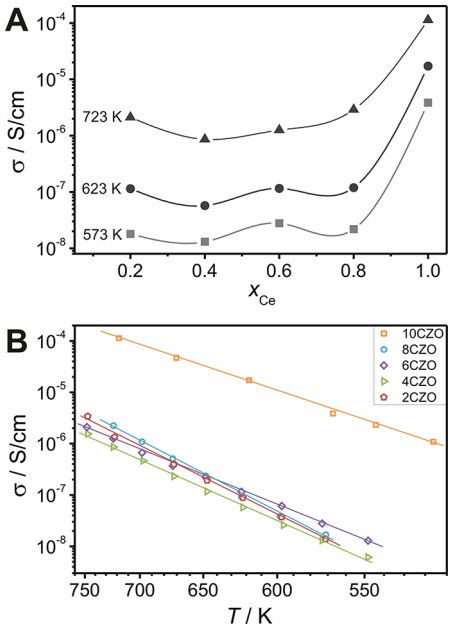

Figure 7. Conductivity measured in air as a function of both film composition (A) and temperature (B). It should be noted that the point connecting lines are not fits to the data.

and Figure 7B shows the temperature dependency for all materials in Arrhenius-type plots.

The CeO_2 thin films revealed by far the highest conductivity values at all temperatures. The different solid solutions showed comparable conductivities with a minimum for 4CZO. For ZrO_2, no data were collected because the pore structure could not be maintained at elevated temperatures, in particular, after prolonged heating periods. From Figure 7B, it is evident that all samples employed in this work follow a simple Arrhenius-type behavior in the temperature range investigated (here 250 °C < ϑ < 600 °C). The activation energy E_a was determined according to the relation $\ln(\sigma_T) = \ln(A) - E_a/k_BT$. Bare CeO_2 showed the lowest activation energy of approximately 0.8 eV, and the solid solutions revealed values ranging from 1.0 eV to 1.3 eV; no obvious trend was observed. In addition, Figure S11 presents the conductivity *versus* temperature data for two different samples of the same initial composition. These data emphasize the reproducibility of the experiments; virtually the same results were obtained.

Chiodelli *et al.* investigated the conductivity properties of CeO_2-ZrO_2 ceramics with a grain size of several micrometers and compositions ranging from 10CZO to 1.6CZO as a function of both the temperature and the oxygen partial pressure. In addition, they determined the transference numbers of electrons and ions *via* electromotive force measurements.[42] For the total conductivity (see Figure 7) as a function of composition, they observed no clear trend, too, even though there was a conductivity minimum between 3CZO and 4CZO, in agreement with our results. The activation energies were found to be 0.86 eV for bare CeO_2 and 0.91−1.34 eV for the solid solutions, which is also consistent with our results. The absolute conductivity values for the microcrystalline solid solutions were lower by a factor of 5−10 compared to the mp-CZO materials. However, our CeO_2 thin films showed a much higher conductivity (by approximately 3 orders of magnitude); structuring at the nanoscale and the related higher oxygen deficiency apparently leads to a strong increase in conductivity.

Tschöpe *et al.* examined the conductivity of CeO_2 as a function of grain size. They showed that the electronic conductivity increases from below 10^{-6} S/cm for 100 nm grains to approximately 2×10^{-4} S/cm for 10 nm grains at 500 °C in air. These findings were supported by calculations assuming positive space charges in the grain boundaries.[15] In microcrystalline bulk materials, such positive space charge results in a concentration increase of the electronic charge carriers and a concentration decrease of the oxygen vacancies in the grain boundaries, leading to both a higher electronic and a lower ionic conductivity in these regions. The bulk (grain interior) conductivities are supposed to be not affected by space charges. However, for nanoscale grains, it is assumed that the space charges overlap with the grain interior, leading to a significant net increase in the electronic conductivity and a decrease in the ionic conductivity. It could also be shown that defect concentration in CeO_2 thin films increases by 3 orders of magnitude by reducing grain sizes from 100 nm down to 10 nm, well in line with the observed increased conductivity.[43] As a result, it is possible to change the character of CeO_2 from a mixed ionic electronic conductor (MIEC) to a predominantly electronic conductor with a high total conductivity simply by reducing the grain size of the material. As shown above, the average domain size of the crystallites of the mp-CeO_2 thin films is 8 nm, and from the temperature-dependent impedance measurements (ϑ_{max} = 450 °C), we determined a conductivity of 3×10^{-4} S/cm at 500 °C, which is in good agreement with both the experimental data and the model by Tschöpe *et al.* for bulk nanocrystalline material.

Compared to bulk nanocrystalline material, the open 3D framework of the mesoporous materials allows immediate manipulation of the redox state and the related properties of all nanocrystals virtually at the same time *via* exposure to different gas atmospheres. In this regard, it is important to note that, apart from the temperature, knowledge about the effect of the gas atmosphere (*i.e.*, either reducing or oxidizing) on the conductivity is also crucial for electrochemical applications. We therefore measured impedance spectra at a constant temperature of approximately 300 °C while varying the oxygen concentration in the sample environment by using mixtures of argon and synthetic air or oxygen (see Figure 8A). The oxygen partial pressure was measured downstream by an YSZ-based EMF cell. We note that both mesoporous CeO_2 and ZrO_2 were not investigated because of the limited thermal stability of these materials; the cubic pore structures collapsed during thermal treatment for several days. Such treatment was necessary to ensure equilibration of the materials with the gas phase at each oxygen partial pressure.

For 8CZO, 6CZO, and 4CZO, the conductivity increased with decreasing oxygen partial pressure (*i.e.*, in reducing atmosphere), and a linear relationship is found when a double-logarithmic scale is applied. In contrast, 2CZO showed virtually no change in conductivity upon reduced oxygen partial pressures. For experimental reasons, it was not possible to carry out systematic studies at very low oxygen partial pressures. Nonetheless, we measured the electrical conductivity of selected samples in forming gas (5% H_2 in Ar), that is, under a highly reducing atmosphere with $\log(p(O_2)/\text{bar}) < -22$ to compare the impedance data with measurements in argon ($\log(p(O_2)/\text{bar}) \approx -4$). The results obtained are shown in Figure 8B. At very low oxygen partial pressures, a decrease in film resistance (*i.e.*, increase in conductivity) of almost 1 order of magnitude was observed for 2CZO. For 4CZO, the change in conductivity was more pronounced, and

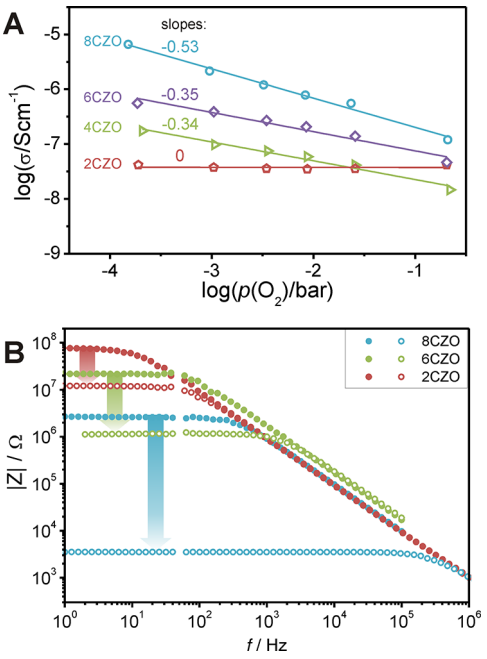

Figure 8. (A) Oxygen partial pressure-dependent conductivity of different mp-CZO thin films. Estimated slopes for a linear relationship between log(σ) and log($p(O_2)$) are shown. Lines correspond to linear fits. (B) Impedance spectra (bode plots) measured both in Ar (solid circles) and highly reducing atmosphere of 5% H_2 in Ar (open circles). The decrease in resistance upon reduction is highlighted by the colored arrows. The data point at f = 50 Hz was removed due to interference with the system voltage. All data points in panels A and B were collected at 300 °C.

mp-CZO thin films with a high cerium content (here 8CZO) even showed an increase in conductivity of almost 3 orders of magnitude.

Mesoporous solids are known to be metastable from a thermodynamic point of view. When studying such highly structured and nanocrystalline materials at elevated temperatures, it is therefore always important to make sure that the microstructure does not change over time due to grain growth, sintering and so forth. GISAXS already provided some insight into the thermal stability of the mp-CZO thin films. To further probe the (kinetic) stability, we calcined selected samples at elevated temperatures to find out whether they undergo changes both in the micro- and nanostructure as well as in the electrical conductivity. For example, a mesoporous 8CZO thin film was first heated at 600 °C for 1 h followed by another aging at 450 °C for 30 h. During this time, the resistance was continuously monitored, as shown in Figure S12 (see Supporting Information). The same sample was also examined by SEM and WAXD. Recorded diffraction patterns did not indicate any changes in crystallinity or grain size. Also, top view SEM images did not indicate a restructuring of the pore network at the air/solid interface. However, the conductivity of the material continuously decreased even after 30 h, thereby presumably indicating slow chemical or structural relaxation processes in the material.

Lastly, we also examined whether humidity has an influence on the conductivity. To do so, we carried out impedance spectroscopy measurements in dry air (dried with silica gel) and humidified air (saturated with water at room temperature). Figure S13 (see Supporting Information) shows impedance spectra along with temperature-dependent conductivity values for a mesoporous 6CZO thin film in both atmospheres. It can be clearly seen that the sample impedance at 350 °C is reduced by more than 50% and that the effect of humidity is non-negligible for all temperatures of interest but decreases with increasing temperature. This result is consistent with studies by Maier *et al.* who observed proton conductivity in nanocrystalline CeO_2 when exposed to humid air.[44] We thus conclude that reproducible measurements rely on a careful control of the humidity.

Defect Chemical Model. On the basis of our experimental results, we propose in the following a defect chemical model for electric transport in mesoporous thin films of the solid solution CeO_2–ZrO_2, especially accounting for both the high specific surface area and the nanocrystalline wall structure. We emphasize that this model is plausible but still has to be proven by further experiments or theory. We also like to emphasize that the point defect model does not account for a possible contribution of proton conduction of the material. As shown in Figure 8 and Figure S13, the influence of $p(H_2O)$ is small compared to $p(O_2)$. As usual for $p(O_2)$-dependent defect studies, we always applied dry gases to the system, and the actual $p(H_2O)$ was not monitored. The $p(H_2O)$-dependent measurements require an even more complex experimental setup, and thus, they will be part of future studies.

In oxide ceramics, the $p(O_2)$ dependence of the conductivity is related to a change in concentration of the mobile ionic and electronic charge carriers (*i.e.*, vacancies, interstitials, electrons, holes). Because most oxides have large electronic band gaps, the concentration of electronic carriers is determined by extrinsic defects in the crystal lattice rather than by thermal interband excitation. Such defects are introduced by either doping with acceptors or donors or by reaction with reducing or oxidizing gas atmospheres (*i.e.*, by controlling the nonstoichiometry). The concentration of mobile ionic charge carriers also depends on the intrinsic defect equibria, such as the anion Frenkel equilibrium and extrinsic defects.

According to the well-established point defect model for fluorite-type oxides such as ZrO_2, CeO_2, and CeO_2–ZrO_2, chemical reduction leads to the release of lattice oxygen (O_O^x) from the bulk of the crystal and, therefore, to the generation of six crystal defects per oxygen molecule, that is, two oxygen vacancies ($V_O^{\bullet\bullet}$) and four electrons:[45]

$$2O_O^x \rightleftharpoons O_{2(g)} + 2V_O^{\bullet\bullet} + 4e' \quad (1)$$

For bulk defects, it is typically assumed that oxygen vacancies are doubly positively charged (with respect

to the crystal lattice), and further, they are known to be responsible for the transport of oxygen ions through the crystal lattice; excess electrons are supposed to be located at the cerium sites as Ce^{3+} (polaron model).[46] When full ionization of the ionic defect is accepted and ideal solution behavior is assumed, the electroneutrality condition is $2[V_O^{\bullet\bullet}] = [e']$ and the law of mass action leads directly to the concentration of electrons (referred to as $[e]$ and oxygen vacancies as $[V_O^{\bullet\bullet}]$ in the following) as a function of $p(O_2)$.

$$\begin{aligned} K_{red} &= [V_o^{\bullet\bullet}]^2 \cdot [e]^4 \cdot p_{O_2} \\ [e] &= 2[V_o^{\bullet\bullet}] \sim K_{red}^{1/6} \cdot (p_{O_2})^{-1/6} \end{aligned} \tag{2}$$

One finds that both $[e]$ and $[V_O^{\bullet\bullet}]$ change with $p(O_2)$ raised to the power of $-1/6$. When constant charge carrier mobility is assumed, the electrical conductivity follows the same dependence. The $p(O_2)$ range for which this behavior is observed is often denoted as the extrinsic region because the defect concentration is controlled by the equilibrium of the material with the surrounding gas atmosphere.

However, in a certain range of $p(O_2)$, when the concentration of extrinsic defects becomes small, a different $p(O_2)$ dependence can be found due to significant amounts of impurities or intrinsic entropy-driven defect equilibria with small defect formation enthalpies. Here the values for the oxygen nonstoichiometry δ are estimated to range from 0.05 to 0.16 for the mesoporous thin films (see Figure 5) if we assume that Ce^{3+} ions (electrons) are compensated by oxygen vacancies. For bulk materials, these values are achieved only under highly reducing conditions and, therefore, an "intrinsically" high defect concentration has to be assumed.[37] The concentration of oxygen vacancies is thus intrinsically large and therefore—in a certain range of $p(O_2)$—considered as being constant. In this case, the concentration of electrons $[e]$ shows a stronger dependence on $p(O_2)$:

$$\begin{aligned} K_{red} &= [V_O^{\bullet\bullet}]^2 \cdot [e]^4 \cdot p_{O_2} \\ [V_O^{\bullet\bullet}] &= \text{const.} \\ [e] &\sim (p_{O_2})^{-1/4} \end{aligned} \tag{3}$$

The concentration of electrons increases with an exponent of $-1/4$ for $p(O_2)$. The corresponding $p(O_2)$ range is often denoted as the intrinsic region because the major defect concentration, here $[V_O^{\bullet\bullet}]$ is determined by intrinsic defects and not by equilibrium with the environment.

At this point, we note again that we did not measure the defect concentrations directly but rather the electrical conductivity σ of the materials as a function of $p(O_2)$. The partial conductivity σ_i caused by the charge carrier i is the product of the charge carrier concentration c_i, the mobility μ_i of the charge carrier, and its charge $z_i e_0$ (*i.e.*, $\sigma_i = |z_i| e_0 \mu_i c_i$). Then, the total conductivity of the material σ_{tot} is the sum of all partial conductivities. In the following, it is assumed that only the conductivity of both the electrons σ_e and the oxygen vacancies σ_V contributes to the total conductivity. For the extrinsic region, all of this yields the following equation for the total conductivity:

$$\begin{aligned} \sigma_{tot} &= \sigma_V + \sigma_e \\ \sigma_{tot} &= 2e_0 \cdot \mu_V \cdot [V_O^{\bullet\bullet}] + e_0 \cdot \mu_e [e] \end{aligned} \tag{4}$$

With eqs 2 and 4 it follows that:

$$\sigma_{tot} \propto (\mu_V + \mu_e) \cdot (p_{O_2})^{-1/6} \tag{5}$$

This shows that the total conductivity is proportional to $p(O_2)$ raised to the power of $-1/6$.

For the intrinsic region, the total conductivity is given by eq 4 combined with eq 3, keeping in mind that $[V_O^{\bullet\bullet}]$ is independent of $p(O_2)$.

$$\sigma_{tot} \propto \mu_V \cdot [V_O^{\bullet\bullet}] + \mu_e \cdot (p_{O_2})^{-1/4} \tag{6}$$

For fluorite-type oxides, we typically find that $[V_O^{\bullet\bullet}] \gg [e]$, and thus, these materials show mostly ionic conductivity in the intrinsic region which, in turn, is independent of the oxygen partial pressure. As shown in Figure 8B, the conductivity of the material increases by 1 order of magnitude when exposed to Ar/H_2 gas mixture. This shows that a hypothetically complete reduction of the material at high $p(O_2)$, which would lead to a constant and dominant electronic conductivity, can be ruled out. Only if the mobility of the oxygen vacancies μ_V is negligibly small for a given material, the total conductivity depends on $p(O_2)$ with an exponent of $-1/4$. It is important to note that this behavior was reported by Mason *et al.* for nanocrystalline 7.5CZO ceramics.[22]

Lee *et al.* measured the $p(O_2)$-dependent conductivity of microcrystalline ceramics of CeO_2–ZrO_2 in the temperature range from 800 to 1100 °C.[47] For both bare CeO_2 and solid solutions containing at least 50% of CeO_2, they observed a linear relationship between the logarithm of the conductivity and the logarithm of $p(O_2)$ with a slope of approximately $-1/6$. This observation agrees well with the classical point defect model for the extrinsic region (see eq 5). The fact that the materials can be described quite well by the simple point defect model over a wide range of $p(O_2)$ (10^{-1} to 10^{-15} atm) indicates the high purity of the samples or, in other words, the low intrinsic defect concentration. However, for the solid solution with only 12% of CeO_2, Lee and co-workers observed no change in conductivity over a wide range of $p(O_2)$ and explained this behavior by predominant ionic conduction. They suggested that the larger cerium ions incorporated in the ZrO_2 lattice facilitate the intrinsic formation of oxygen vacancies and lead to higher concentrations of Frenkel defects. For 2CZO, we also find a $p(O_2)$-independent conductivity, which is consistent with the results of

Lee *et al.* and the assumption of predominant ionic conductivity. For mp-CZO thin films with a higher cerium content, however, we determine exponents ranging between −1/3 and −1/2, significantly higher than −1/4 observed by Mason *et al.* for 7.5CZO. To explain this result, we need to consider the specific microstructure of our samples. In the ideal (bulk) point defect model, it is assumed that, by oxygen release upon chemical reduction, vacancies are generated on random sites in the interior of a crystal with virtually infinite dimensions. In this particular case, all of the metal cations are formally characterized by the charge number of +4 while the ion charge number of oxygen is −2. The release of one oxygen atom leads to the formation of a vacancy with the relative charge number of +2 and two excess electrons, represented by two M^{3+} cations in the polaron picture. In the vicinity of the material surface, this defect model is too simple because unsaturated bonds and/or adsorbed gas molecules lead to different effective charges of (near) surface atoms. This fact can be neglected for ceramics with large grains and a small surface area-to-volume ratio. In our materials, however, a significant fraction of atoms are located at or very close to the surface. XPS data clearly show that the mp-CZO thin films contain large amounts of Ce^{3+}. In the following, we therefore make the formal assumption that a formed oxygen vacancy can be described by a mean charge number of n (with $n \leq 2$), assuming incompletely ionized vacancies with respect to the treatment for bulk defects. The release of one oxygen molecule then leads to the formation of two vacancies with $2n$ excess electrons, and the law of mass action yields the following equation:

$$K_{red} = [V_O^{n\bullet}]^2 \cdot [e]^{2n} \cdot p_{O_2} \quad (7)$$

Now, we can describe the total conductivity of the material in analogy to eqs 5 and 6 for the extrinsic region ($[e] = n[V_O^{n\bullet}]$) with

$$\sigma_{tot} \propto (\mu_V + \mu_e) \cdot (p_{O_2})^{-1/2(n+1)} \quad (8)$$

and the intrinsic region ($[V_O] \approx$ const) with

$$\sigma_{tot} \propto \mu_V \cdot [V_O] + \mu_e \cdot (p_{O_2})^{-1/2n} \quad (9)$$

Exponents between −1/3 and −1/2 can only be obtained if the oxygen vacancy has a charge number of $0 \leq n \leq 0.5$ and $1 \leq n \leq 1.5$ for the extrinsic and intrinsic regions, respectively.

For the intrinsic region, we need to assume that the oxygen vacancies have a negligibly small mobility, as proposed by Mason *et al.* The fact that the predominantly ion-conducting 2CZO material showed no change in conductivity indicates that the $p(O_2)$ range investigated may correspond to the intrinsic region for all samples and that the effective charge of the oxygen vacancies is greater than or equal to 1 but smaller than or equal to 1.5. The assumption that oxygen vacancies represent the major defect type in microcrystalline materials and that these vacancies are not able to move in the crystal lattice appears contradictory at first glance because a minimum mobility is required for their formation. However, in mesoporous materials with a nanocrystalline wall structure, a large fraction of the oxygen atoms is located near the solid/gas interface and the network of open pores leads to the fact that basically all grains (in an extended sample) are exposed to the gas phase. To contribute to the total conductivity, oxygen vacancies need to cross grain boundaries that are supposed to be blocking interfaces for the vacancy transport mechanism. Furthermore, experiments conducted by Esch *et al.* on CeO_2 single-crystal surfaces showed that surface oxygen vacancies tend to form linear clusters or trimers together with subsurface vacancies. These vacancy clusters are surrounded by Ce^{3+} ions.[48] The formation of such clusters further suppresses the mobility of the oxygen vacancies.

In summary, there are two possible explanations for the origin of oxygen vacancies with a relative charge number lower than +2. (i) Because of the significant amount of reduced cerium species (Ce^{3+}), further excess electrons formed due to removal of an O^{2-} anion are not located on Ce^{4+} but at least in parts on the oxygen vacancy site. For $n = 1$, on average, one electron is located on a vacancy site which would correspond to a color center. Those have been introduced for strongly reduced ceria single crystals by Tuller *et al.*[11]

$$V_O^{\bullet\bullet} + xe' \rightleftharpoons V_O^{(2-x)\bullet} \quad (10)$$

Alternatively, the formation of associated defects formed by oxygen vacancies and reduced Ce ions is considered (essentially also leading to vacancies with a lower formal charge number than +2):[37,49]

$$\begin{aligned} n &= 1 \quad V_O^{\bullet\bullet} + Ce'_{Ce} \rightleftharpoons (V_O^{\bullet\bullet}Ce'_{Ce})^{\bullet} \\ n &= 0 \quad V_O^{\bullet\bullet} + 2Ce'_{Ce} \rightleftharpoons (Ce'_{Ce}V_O^{\bullet\bullet}Ce'_{Ce})^{x} \end{aligned} \quad (11)$$

(ii) Hypothetically, another model could be introduced: while O^{2-} ions are the predominant oxygen species in the bulk material stabilized by the interaction with counterions, in the vicinity of the surface, the oxygen anions may carry a lower charge and, therefore, oxygen release from the surface would lead to the formation of vacancies with a charge number lower than +2. In this case, the Ce^{3+} species, as verified by XPS, were not compensated by intrinsic oxygen vacancies, but by O^- obeying the AO_2 fluorite structure: $Ce^{3+}(O^{2-}O^-)$ or $Ce^{3+}(O^{2-}OH^-)$ taking hydroxide groups at the surface into account.

To verify these assumptions, either the valence state of the lattice oxygen needs to be investigated *via* spectroscopy or the partial conductivity of the oxygen vacancies needs to be measured as a function

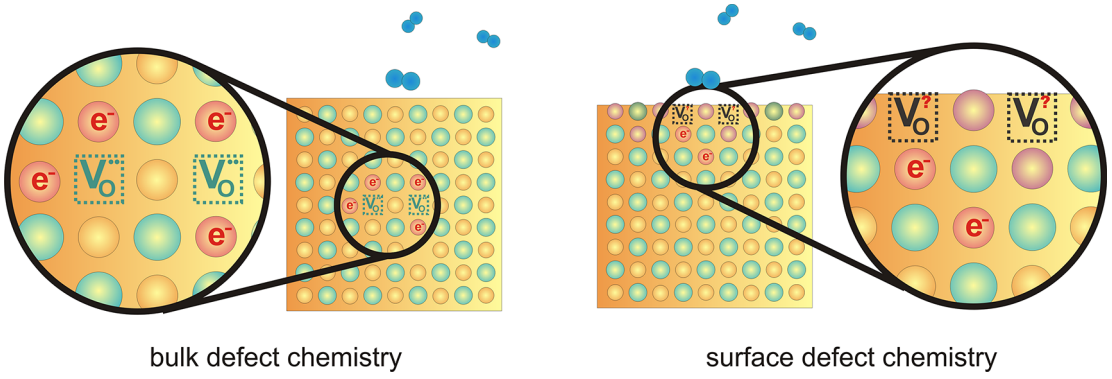

Figure 9. Comparison of the conventional bulk and the proposed surface defect chemical model for the release of oxygen from the crystal lattice, *i.e.*, reduction of the material. O^{2-} and Ce^{4+} ions on lattice sites are shown in cyan and orange, respectively. In the bulk defect chemical model, the removal of an oxygen molecule leads to the formation of two oxygen vacancies and four excess electrons or four reduced ceria species. In contrast, when surface chemistry determines the material properties, the release of oxygen may lead to a different defect formation because effective charges of lattice and/or defect sites differ from those in the bulk.

of $p(O_2)$ to determine the effective charge of the vacancies (Figure 9). At this point, we have no experimental evidence which allows deciding for one explanation over the other.

CONCLUSION

Ordered mesoporous thin films of $Ce_xZr_{1-x}O_2$ with six different compositions ranging from bare CeO_2 to ZrO_2 were synthesized *via* facile polymer templating. Characterization of the nanoscale structure and the morphology using various state-of-the-art techniques indicated that the mp-CZO materials employed in this work are homogeneous on both the micro- and the nanoscale and are structurally highly stable even up to 600 °C for several hours. Therefore, we consider mp-CZO as a perfect model system for the study of point defect chemistry in nanocrystalline and nonstoichiometric oxides with a high surface area. The charge transport properties of these model-type mp-CZO films were analyzed under well-defined conditions as a function of the temperature, oxygen partial pressure, and composition using impedance spectroscopy. The data obtained show that the high surface area of the nanocrystalline materials leads to properties that are quite different from those reported for nonporous and microcrystalline ceramics. When changing the oxygen partial pressure in the environment, the observed change in conductivity deviates strongly from the classical point defect models for binary oxides. We therefore suggest a novel "surface" defect model taking into account that effective charges of the lattice ions near the surface may differ from the bulk phase. Using this model, our experimental results lead us to conclude that the average charge number of the oxygen vacancies in the walls of mp-CZO thin films is +1.5 to +1 rather than +2 assuming intrinsic defects.

METHODS

Sample Preparation. The synthetic route for the preparation of mp-CZO thin films is adopted from refs 50 and 51. In a small container, 40 mg of $H[(CH_2CH_2)_{0.67}(CH_2CHCH_2CH_3)_{0.33}]_{89}(OCH_2CH_2)_{79}OH$, referred to as KLE,[52] was dissolved in a mixed solvent of ethanol (1.6 mL, 99.8%, VWR) and 2-methoxyethanol (0.4 mL, 99.8%, Sigma-Aldrich). Thereafter, both $CeCl_3 \cdot 7H_2O$ (99.9%, Sigma-Aldrich) and $ZrCl_4$ (99.9%, Sigma-Aldrich) were added, and the solution was stirred for 1 h. For all materials prepared in this work, the total salt content in solution was approximately 54 μmol. Ten minutes before film deposition, double distilled water (0.1 mL) was added to the final solution. Thin films were prepared *via* dip-coating on both Si(100) and quartz glass substrates. Optimal conditions included a relative humidity of 20% and constant withdrawal rates of 3−13 mm/s. After film deposition, the samples were first dried in air at 120 °C for 1 h and then heated to 300 °C using a 180 min ramp, followed by another aging for 12 h. Removal of the polymer template and crystallization were achieved by heating the thin films to 600 °C (500 °C for ZrO_2) using a ramp of 10 °C/min, followed by aging for 5−60 min.

Microelectrodes. Two interdigitated Pt microelectrodes with an average electrode distance of approximately 20 μm and an accumulated electrode length of 40 cm were placed on the top surface of the mp-CZO thin films (see Figure S14 in Supporting Information). These microelectrodes were prepared *via* photolithography. First, an approximately 2 μm thick layer of a negative photoresist (ma-N 1420, micro resist technology GmbH) was deposited onto the samples and prebaked at 100 °C for 2 min. Structure transfer was done using a chrome-plated soda lime glass mask and a mask aligner (MA56, Karl Süss) with UV broad band light source (approximately 6 mW/cm^2 at 365 nm). After 85 s of light exposure, the structure was developed using the ma-D 533s developer from micro resist technology GmbH. Metallization was done by pulsed laser deposition using a Pt metal target, a KrF excimer laser at 248 nm, and an Ar background pressure of approximately 10^{-5} mbar. Liftoff was effected by dissolving the photoresist in acetone.

Structural and Compositional Characterization. Scanning electron microscopy (SEM) images were recorded with both a LEO Gemini 982 and a MERLIN high-resolution SEM from Carl Zeiss (Oberkochen, Germany). Samples for SEM imaging were prepared on Si(100) substrates. The film thickness was determined *via* cross-sectional SEM. Energy-dispersive X-ray spectroscopy (EDS) analyses were carried out in combination with SEM using a Si/Li detector from Oxford Instruments. Transmission electron

microscopy (TEM) and scanning TEM (STEM) studies were performed using a Tecnai F30 G^{2}STwin microscope (FEI, 300 kV, FEG cathode, C_S = 1.2 mm, point resolution of 0.2 nm in TEM, point resolution of 0.19 nm in STEM). TEM images were taken with a Gatan Multiscan CCD camera (Gatan), while a high-angle annular dark-field (HAADF) detector (Fischione) was used to collect STEM images. Wide-angle X-ray diffraction (WAXD) measurements were carried out in $\theta-2\theta$ geometry on a Siemens D500 diffractometer. Grazing incidence small-angle X-ray scattering (GISAXS) patterns were collected at the German synchrotron radiation facility HASYLAB at DESY on beamline BW4 using a MarCCD area detector and a sample−detector distance of approximately 1820 mm. The samples were also analyzed by time-of-flight secondary ion mass spectrometry (ToF-SIMS) using a ToF-SIMS 5 from ION-TOF GmbH. A primary ion beam of 25 keV Bi^+ was used to generate secondary ions for analysis. Sputter etching was carried out using a beam of 1 keV O^+. X-ray photoelectron spectroscopy (XPS) measurements were carried out at the Physical Electronics demo lab in Chanhassen, Minnesota, on a VersaProbe PHI 5000 with monochromatic Al Kα X-ray source. All spectra were taken with charge compensation, 100 W energy, and 8 min of measuring time. The excitation was perpendicular to the sample surface, while the analyzer was aligned 45° relative to the sample surface.

Electrical Characterization. Conductivity measurements were carried out in a home-built setup (see Figure S15 in Supporting Information) with tube furnace (LT-14-O, Heraeus) and PID controller (2416, Eurotherm). The actual temperature in the vicinity of the samples was controlled using both a type K thermocouple and a digital multimeter 2700 (Keithley) with reference junction at 50 °C. The mp-CZO thin films with interdigitated Pt electrodes on the top surface were mounted in a sample holder equipped with shielded Pt wiring. The AC conductivity was determined *via* impedance spectroscopy in the frequency range between 100 kHz and 0.1 Hz using a Zahner IM6 electrochemical workstation. For oxygen partial pressure-dependent measurements, the alumina tube of the furnace was equipped with gastight brass flanges. The atmosphere was controlled *via* mass flow controllers from MKS Instruments. The oxygen partial pressure was measured using a home-built zirconia-based EMF cell and a digital multimeter 2700 from Keithley. Gas mixtures of argon and synthetic air or oxygen were used to control the oxygen partial pressure (argon 5.0, oxygen 5.0, Praxair).

Conflict of Interest: The authors declare no competing financial interest.

Acknowledgment. We thank S. Alnabulsi from Physical Electronics Inc. for the XPS measurements, T. Henning for support in the lithography process, and S. O. Steinmueller and M. Falk for the SIMS measurements. T.B. thanks HASYLAB at DESY for beamtime. P.H. is grateful to the Fonds der Chemischen Industrie (FCI) for a scholarship. J.J. acknowledges funding by the DFG (Ja 648/21).

Supporting Information Available: Extended information on the micro- and mesostructure of the materials, including chemical composition (HRTEM, STEM, GISAXS, EDS). Details on the experimental setup for conductivity measurements. This material is available free of charge *via* the Internet at http://pubs.acs.org.

REFERENCES AND NOTES

1. Tilley, R. J. D. *Defects in Solids*, 1st ed.; John Wiley & Sons: Hoboken, NJ, 2008.
2. Maier, J. *Physical Chemistry of Ionic Materials: Ions and Electrons in Solids*, 1st ed.; John Wiley & Sons: New York, 2004.
3. Tuller, H. L. Ionic Conduction in Nanocrystalline Materials. *Solid State Ionics* **2000**, *131*, 143–157.
4. Maier, J. Defect Chemistry and Ion Transport in Nanostructured Materials Part II. Aspects of Nanoionics. *Solid State Ionics* **2003**, *157*, 327–334.
5. Seayad, A. M.; Antonelli, D. M. Recent Advances in Hydrogen Storage in Metal-Containing Inorganic Nanostructures and Related Materials. *Adv. Mater.* **2004**, *16*, 765–777.
6. Rolison, D. R. Catalytic Nanoarchitectures—The Importance of Nothing and the Unimportance of Periodicty. *Science* **2003**, *299*, 1698–1701.
7. Tiemann, M. Porous Metal Oxides as Gas Sensors. *Chem.—Eur. J.* **2007**, *13*, 8376–8388.
8. Long, J. W.; Dunn, B.; Rolison, D. R.; White, H. S. Three-Dimensional Battery Architectures. *Chem. Rev.* **2004**, *104*, 4463–4492.
9. Grätzel, M. Mesoscopic Solar Cells For Electricity and Hydrogen Production from Sunlight. *Chem. Lett.* **2005**, *1*, 8–13.
10. Lupetin, P.; Gregori, G.; Maier, J. Mesoscopic Charge Carrier Chemistry in Nanocrystalline $SrTiO_3$. *Angew. Chem., Int. Ed.* **2010**, *49*, 10123–10126.
11. Tuller, H. L.; Nowick, A. S. Defect Structure and Electrical Properties of Nonstoichiometric CeO_2 Single Crystals. *J. Electrochem. Soc.* **1979**, *126*, 209.
12. Mogensen, M.; Sammes, N.; Tompsett, G. A. Physical, Chemical and Electrochemical Properties of Pure and Doped Ceria. *Solid State Ionics* **2000**, *129*, 63–94.
13. Omata, T.; Goto, Y.; Otsuka-Yao-Matsuo, S. Nanocrystals of Zirconia- and Ceria-Based Solid Electrolytes. *Sci. Technol. Adv. Mater.* **2007**, *8*, 524–530.
14. Chiang, Y.-M.; Lavik, E. B.; Kosacki, I.; Tuller, H. L. Nonstoichiometry and Electrical Conductivity of Nanocrystalline CeO_{2-x}. *J. Electroceram.* **1997**, *1*, 7–14.
15. Tschöpe, A.; Birringer, R. Grain Size Dependence of Electrical Conductivity in Polycrystalline Cerium Oxide. *J. Electroceram.* **2001**, *7*, 169–177.
16. Kim, S.; Maier, J. On the Conductivity Mechanism of Nanocrystalline Ceria. *J. Electrochem. Soc.* **2002**, *149*, J73–J83.
17. Göbel, M. C.; Gregori, G.; Guo, X.; Maier, J. Boundary Effects on the Electrical Conductivity of Pure and Doped Cerium Oxide Thin Films. *Phys. Chem. Chem. Phys.* **2010**, *12*, 14351–14361.
18. Korte, C.; Schichtel, N.; Hesse, D. Janek, Influence of Interface Structure on Mass Transport in Phase Boundaries between Different Ionic Materials—Experimental Studies and Formal Considerations. *J. Monatsh. Chem.* **2009**, *140*, 1069.
19. De Souza, R.; Pietrowski, M. J.; Anselmi-Tamburini, U.; Kim, S.; Munir, Z. A.; Martin, M. Oxygen Diffusion in Nanocrystalline Yttria-Stabilized Zirconia: The Effect of Grain Boundaries. *Phys. Chem. Chem. Phys.* **2008**, *10*, 2067–2072.
20. Yashima, M.; Takashina, H.; Kakihana, M.; Yoshimura, M. Low-Temperature Phase Equilibria by the Flux Method and the Meta-stable Phase Diagram in the ZrO_2-CeO_2 System. *J. Am. Ceram. Soc.* **1994**, *77*, 1869–1874.
21. Lamas, D. G.; Fuentes, R. O; Fabregas, I. O.; Fernandez de Rapp, M. E.; Lascelea, G. E.; Casanova, J. R.; Walöe de Reca, N. E.; Craievich, A. F. Synchrotron X-ray Diffraction Study of the Tetragonal-Cubic Phase Boundary of Nanocrystalline ZrO_2-CeO_2 Synthesized by a Gel-Combustion Process. *J. Appl. Crystallogr.* **2005**, *38*, 867–873.
22. Boaro, M.; Trovarelli, A.; Hwang, J.-H.; Mason, T. O. Electrical and Oxygen Storage/Release Properties of Nanocrystalline Ceria−Zirconia Solid Solutions. *Solid State Ionics* **2002**, *147*, 85–95.
23. Abdollahzadeh-Ghom, S.; Zamani, C.; Nazarpour, S.; Morante, J. R. Oxygen Sensing with Mesoporous Ceria−Zirconia Solid Solutions. *Sens. Actuators, B* **2009**, *140*, 216–221.
24. Abdollahzadeh-Ghom, S.; Zamani, C.; Andreu, T.; Epifani, M.; Morante, J. R. Improvement Oxygen Storage Capacity Using Mesoporous Ceria−Zirconia Solid Solutions. *Appl. Catal., B* **2011**, *108−109*, 32–38.
25. Mamontov, E.; Egami, T.; Brezny, R.; Koranne, M.; Tyagi, S. Lattice Defects and Oxygen Storage Capacity of Nanocrystalline Ceria and Ceria−Zirconia. *J. Phys. Chem. B* **2000**, *104*, 11110–11116.
26. Di Monte, R.; Kasper, J. Heterogenous Environmental Catalysis—A Gentle Art: CeO_2-ZrO_2 Mixed Oxides as a Case History. *Catal. Today* **2005**, *100*, 27–35.

27. Krishan, C. K.; Nakamura, K.; Hirata, H.; Ogura, M. Pt/CeO_2-ZrO_2 Present in the Mesopores of SBA-15—A Better Catalyst for CO Oxidation. *Phys. Chem. Chem. Phys.* **2010**, *12*, 7513–7520.
28. Pijolat, M.; Prin, M.; Soustelle, M.; Touret, O.; Nortier, P. Thermal Stability of Doped Ceria: Experimental and Modelling. *J. Chem. Soc., Faraday Trans.* **1995**, *91*, 3941–3948.
29. Mamontov, E.; Brezny, R.; Koranne, M.; Egami, T. Nanoscale Heterogeneities and Oxygen Storage Capacity of $Ce_{0.5}Zr_{0.5}O_2$. *J. Phys. Chem. B* **2003**, *107*, 13007–13014.
30. Brezesinski, T.; Antonietti, M.; Smarsly, B. M. Self-Assembled Metal Oxide Bilayer Films with "Single-Crystalline" Overlayer Mesopore Structure. *Adv. Mater.* **2007**, *19*, 1074–1078.
31. Haetge, J.; Suchomski, C.; Brezesinski, T. Ordered Mesoporous MFe_2O_4 (M = Co, Cu, Mg, Ni, Zn) Thin Films with Nanocrystalline Walls, Uniform 16 nm Diameter Pores and High Thermal Stability: Template-Directed Synthesis and Characterization of Redox Active Trevorite. *Inorg. Chem.* **2010**, *49*, 11619–11626.
32. Yashima, M.; Sasaki, S.; Yamaguchi, Y.; Kakihana, M.; Yoshimura, M.; Mori, T. Internal Distortion in ZrO_2-CeO_2 Solid Solutions: Neutron and High Resolution Synchrotron X-ray Diffraction Study. *Appl. Phys. Lett.* **1998**, *72*, 182–184.
33. Shannon, R. D.; Prewitt, C. T. Effective Ionic Radii in Oxides and Fluorides. *Acta Crystallogr.* **1969**, *B25*, 925–946.
34. Patterson, A. L. The Scherrer Formula for X-ray Particle Size Determination. *Phys. Rev.* **1939**, *56*, 978–982.
35. Burroughs, P.; Hamnett, A.; Orchard, A. F.; Thornton, G. Satellite Structure in the X-ray Photoelectron Spectra of Some Binary and Mixed Oxides of Lanthanum and Cerium. *J. Chem. Soc., Dalton Trans.* **1976**, *17*, 1686–1698.
36. Romeo, M.; Bak, K.; El Fallah, J.; Le Normand, F.; Hilaire, L. XPS Study of the Reduction of Cerium Dioxide. *Surf. Interface Anal.* **1993**, *20*, 508–512.
37. Duncan, K. L.; Wang, Y.; Bishop, S. R.; Ebrahimi, F.; Wachsman, E. D. The Role of Point Defects in the Physical Properties of Nonstoichiometric Ceria. *J. Appl. Phys.* **2007**, *101*, 044906.
38. Moos, R.; Wedemann, M.; Spörl, M.; Reiss, S.; Fischerauer, G. Direct Catalyst Monitoring by Electrical Means: An Overview on Promising Novel Principles. *Top. Catal.* **2009**, *52*, 2035–2040.
39. Irvine, J. T. S.; Sinclair, D. C.; West, A. R. Electroceramics: Characterization by Impedance Spectroscopy. *Adv. Mater.* **1990**, *2*, 132–138.
40. Peters, A.; Korte, C.; Hesse, D.; Zakharov, N.; Janek, J. Ionic Conductivity and Activation Energy for Oxygen Ion Transport in Superlattices—The Multilayer System CSZ $(ZrO_2+CaO)/Al_2O_3$. *Solid State Ionics* **2007**, *178*, 67–76.
41. Hertz, J. L.; Tuller, H. L. Measurement and Finite Element Modeling of Triple Phase Boundary-Related Current Constriction in YSZ. *Solid State Ionics* **2007**, *178*, 915–923.
42. Chiodelli, G.; Flor, G.; Scagliotti, M. Electrical Properties of the ZrO_2-CeO_2 System. *Solid State Ionics* **1996**, *91*, 109–121.
43. Kosacki, I.; Suzuki, T.; Anderson, H. U.; Colomban, P. Raman Scattering and Lattice Defects in Nanocrystalline CeO_2 Thin Films. *Solid State Ionics* **2002**, *149*, 99–105.
44. Shirpour, M.; Gregori, G.; Merkle, R.; Maier, J. On the Proton Conductivity in Pure and Gadolinium Doped Nanocrystalline Cerium Oxide. *Phys. Chem. Chem. Phys.* **2011**, *13*, 937–940.
45. Panlener, R. J.; Blumenthal, R. N.; Garnier, J. E. A Thermodynamic Study of Nonstoichiometric Cerium Dioxide. *J. Phys. Chem. Solids* **1975**, *36*, 1213–1222.
46. Tuller, H. L.; Nowick, A. S. Small Polaron Electron Transport in Reduced CeO_2 Single Crystals. *J. Phys. Chem. Solids* **1977**, *38*, 859–867.
47. Lee, J.-H.; Yoon, S. M.; Kim, B.-K.; Lee, H.-W.; Song, H. S. Electrical Conductivity and Defect Structure of CeO_2-ZrO_2 Mixed Oxide. *J. Mater. Sci.* **2002**, *37*, 1165–1171.
48. Esch, F.; Fabris, S.; Zhou, L.; Montini, T.; Africh, C.; Fornasiero, P.; Comelli, G.; Rosei, R. Electron Localization Determines Defect Formation on Ceria Substrates. *Science* **2005**, *309*, 752–755.
49. Otake, T.; Yugami, H.; Yashiro, K.; Nigara, Y.; Kawada, T.; Mizusaki, J. Nonstoichiometry of $Ce_{1-x}Y_xO_{2-0.5x-\delta}$ ($x = 0.1, 0.2$). *Solid State Ionics* **2003**, *161*, 181–186.
50. Brezesinski, T.; Antonietti, M.; Groenewolt, M.; Pinna, N.; Smarsly, B. The Generation of Mesostructured Crystalline CeO_2, ZrO_2, and CeO_2-ZrO_2 Films Using Evaporation–Induced Self-Assembly. *New J. Chem.* **2005**, *29*, 237–242.
51. Brezesinski, T.; Wang, J.; Senter, R.; Brezesinski, K.; Dunn, B.; Tolbert, S. H. On the Correlation between Mechanical Flexibility, Nanoscale Structure, and Charge Storage in Periodic Mesoporous CeO_2 Thin Films. *ACS Nano* **2010**, *4*, 967–977.
52. Thomas, A.; Schlaad, H.; Smarsly, B.; Antonietti, M. Replication of Lyotropic Block Copolymer Mesophase into Porous Silica by Nanocasting: Learning about Finer Details of Polymer Self-Assembly. *Langmuir* **2003**, *19*, 4455–4459.